Hard photon production in $p+^{197}$Au reaction at $E_p=27$ MeV

D. R. Chakrabarty and V. M. Datar
Nuclear Physics Division, Bhabha Atomic Research Centre, Mumbai 400 085, India

Y. K. Agarwal, C. V. K. Baba, and M. S. Samant*
Tata Institute of Fundamental Research, Mumbai 400 005, India

I. Mazumdar,† A. K. Sinha, and P. Sugathan
Nuclear Science Centre, New Delhi 110 067, India
(Received 20 January 1999; published 9 July 1999)

Gamma ray spectra in the range of $\sim 8-35$ MeV have been measured at 45°, 90°, and 135° in the reaction $p+^{197}$Au at $E_p=27$ MeV. The statistical and the nucleon-nucleon bremsstrahlung models fail to describe the data. The direct-semidirect capture model works well for $E_\gamma > 20$ MeV. The possibility of extracting information on the single particle strength distribution in the final nucleus has been illustrated.
[S0556-2813(99)00108-9]

PACS number(s): 25.40.Lw, 21.10.Pc, 24.30.Cz, 27.80.+w

I. INTRODUCTION

Production of high energy gamma rays ($E_\gamma \sim 5-20$ MeV) in low energy heavy ion ($A>12$, $E_{\rm beam}/A < 8$ MeV) fusion reactions is well understood in terms of the statistical model incorporating the giant dipole resonance built on excited states. Many experiments in this beam energy regime have revealed interesting nuclear structure features such as shape evolution and shape fluctuation of hot rotating nuclei. At much higher beam energies ($E_{\rm beam}/A > 20$ MeV) there appears in the spectrum a so-called hard ultradipole tail for E_γ greater than about 20 MeV. This again is reasonably understood in terms of the nucleon-nucleon bremsstrahlung originating from the initial stages of the reaction. These hard photons have been observed [1,2] also in low energy alpha and ^{3}He-induced reactions down to $E_{\rm beam} \sim 27$ MeV and are, however, not yet well understood.

Hard photon production in proton induced reactions at high energies (beyond $E_{\rm beam}=70$ MeV) has been studied experimentally [3–5] and the nucleon-nucleon bremsstrahlung mechanism is reasonably successful in explaining the data. There are not many experiments done at low beam energies and some measurements [6] near $E_p=35$ MeV have revealed that the production cross section of hard photons is much higher than the prediction of the bremsstrahlung model. A systematic study of the proton-induced hard photon production in this energy range is important. These will be useful, for example, in any attempt to understand [1] the alpha-induced reaction data by folding the experimental proton-induced data. In any case a proper understanding of the proton-induced data is necessary before the hard photon production in more complex particle-induced reactions is sought to be understood.

Radiative capture of nucleons to specific final states at low excitation energies (E_X) and the beam energy dependence of the cross section has been studied for many systems. This has been explained in terms of the direct-semidirect (DSD) mechanism [7,8] where the incoming proton is captured either directly or via the intermediate excitation of a giant resonance into a final single particle configuration. In a recent work the DSD model has been extended to capture to unbound states and it is shown [9] to work well for the $p+^{89}$Y system at $E_p \sim 20$ MeV. In these calculations, besides the relevant giant resonance strength function, the important ''effective'' input is the energy and the widths of the single particle states. In other words, if this model is really successful in general, it can be utilized in the appropriate beam and gamma ray energy range to extract information on the single particle strengths and their damping in heavy nuclei. This type of information has been traditionally obtained from particle transfer reactions and more recently, also, through $(e,e'N)$ reactions using high duty cycle electron accelerators. The radiative capture and $(e,e'N)$ experiments should have an advantage over the transfer experiments because one of the interaction vertices is well understood. However, in the case of radiative capture, a systematic study of the success (or failure) of the DSD model is very important before this is exploited.

In this paper we report a study of the hard photon production in proton-induced reactions on ^{197}Au at $E_p=27$ MeV, with the various motivations described above. The experimental details are presented in Sec. II. In Sec. III, the results of the statistical and nucleon-nucleon bremsstrahlung model calculations will be presented. In Sec. IV, we describe the DSD model calculation including capture to continuum states. Our method of calculation uses a more simple minded approach compared to that of Parker *et al.* [9]. We shall discuss the extent of success of this model along with an attempt to extract information on the single particle damping mechanism. Section V presents the summary of the present work along with a few conclusions.

*Present address: SCADA System Division, NELCO, Andheri, Mumbai-400 093.

†Present address: Department of Physics, SUNY, Stony Brook, NY 11794.

II. EXPERIMENTAL MEASUREMENTS

The experiment was performed at the 15UD Pelletron accelerator laboratory at the Nuclear Science Center at Delhi using a 27 MeV pulsed proton beam. The beam pulses, which were ~ 0.5 nsec wide and repeated every 250 nsec, bombarded a self-supporting gold foil (purity $>99.99\%$) of thickness 14 mg/cm^2. This target was made by rolling and its thickness was measured by weighing. Two kinds of detectors were used for the gamma ray measurements. For the spectral measurement a 25 cm diameter$\times$30 cm deep NaI(Tl) detector [10] (with seven 7.6 cm diameter Hamamatsu R1307-07 photomultiplier tubes viewing the scintillator) was placed at 60 cm from the target and at 90° to the beam direction. The detector was surrounded by an active 7.6 cm thick BC-400 [10] plastic shield for vetoing cosmic ray events. A 10 cm thick outer lead shield reduced the gamma ray background while boric acid and lithium carbonate were used to reduce the neutron background [11]. A thick lead aperture of diameter 17 cm was put coaxially in front of the detector to illuminate only the central part of the detector for good energy response. In addition a thin lead sheet (5 mm thick) covered the front face to cut down low energy photons. For the angular distribution measurement two 20 cm long BaF_2 detectors of hexagonal cross section with opposite side distance of 9 cm [12] were used. The BaF_2 detectors were interchangeably placed at 45°, 90°, and 135° at a distance of about 40 cm from the target. They had lead apertures of diameter 6 cm and ~ 5 mm lead sheets in front. The BaF_2 detectors were thermally insulated to keep the temperature reasonably constant.

Energy calibration of all the detectors was done by detecting the 4.43, 6.13, and 15.1 MeV gamma rays arising from the inelastic scattering of protons from ^{12}C and ^{16}O in a 5.5 mg/cm^2 Mylar target. The high voltages on the photomultiplier tubes were kept low to ensure linearity of calibration up to ~ 40 MeV. The Doppler correction to the observed gamma energies and also the peak position expected from the electron gamma shower calculation using the code EGS4 [13] (important for the 15.1 MeV line) were employed while extracting the calibration constants. In calculating the Doppler correction, the angular distribution effect of the proton inelastic scattering was incorporated, utilizing the already published data [14,15] on these measurements. The calibration of all the detectors was checked at regular intervals by pushing in the Mylar target in the beam path. As expected the NaI(Tl) detector calibration was stable to $\pm 0.2\%$ while that of the BaF_2 detectors within $\pm 2.5\%$ and $\pm 3.3\%$ over a period of 3 days. This was taken care of while summing spectra from different runs.

The separation of the neutron and gamma induced events in each detector was achieved by measuring their time of flight (TOF) with respect to the beam burst. The pileup was measured using the standard pulse shape discrimination method [1] by measuring the zero crossover time (ZCOT) of the bipolar pulse from the amplifier. Experimental data were recorded in list mode using a CAMAC-based data acquisition system. The three parameters measured for each detector per event were the energy deposited in the detector, the TOF, and the ZCOT. The TOF resolutions for the NaI(Tl) and BaF_2 detectors for energy deposits of >15 MeV were ~ 1.8 and 0.8 nsec, respectively. Typical TOF spectra for the NaI(Tl) and BaF_2 detectors are shown in Fig. 1. As can be seen the neutron-gamma separation was unambiguous in both the detectors. At the highest energy windows shown in the figure the gamma yield is significantly higher than the cosmic ray background in the prompt peak. This cosmic ray background is somewhat higher in the BaF_2 detector compared to that in the NaI(Tl) because of the absence of an active cosmic shield in the former. Typical ZCOT spectra for the two detectors are shown in Fig. 2. The contribution of pileup events under the nonpileup peak in the NaI(Tl) detector ($\sim 10\%$ for $E_\gamma \sim 12$ MeV, $\sim 7\%$ for $E_\gamma \sim 15$ MeV, and $\sim 3\%$ for $E_\gamma > 18$ MeV) was corrected for in the off-line data analysis. The pileup effect in BaF_2 detectors is much smaller than in NaI(Tl). This is because of the smaller size as well as the lower thermal neutron capture probability in BaF_2.

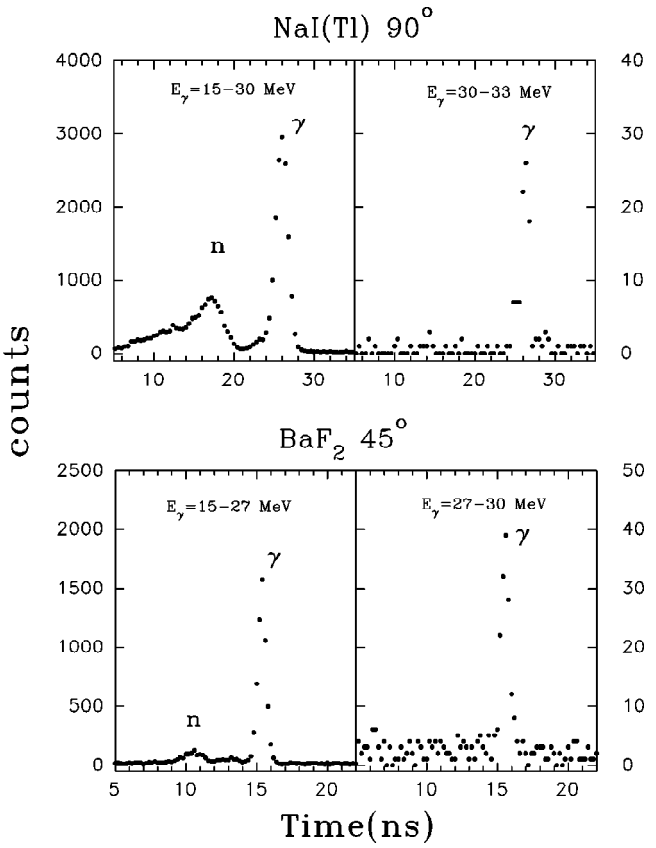

FIG. 1. Typical TOF spectra for the NaI(Tl) detector at 90° and a BaF_2 detector at 45° for the energy gates shown in the figure.

The response of the NaI(Tl) detector was earlier measured [11] using various gamma rays of energies between 4 and 23 MeV originating from radioactive sources, $(p,p'\gamma)$ reaction on ^{12}C and ^{11}B(p,γ) reaction and compared with the EGS4 calculations. The comparisons of the measured 15.1 MeV gamma spectra from the ^{12}C$(p,p'\gamma)$ reaction in the present experiment with the EGS4 calculation, for both NaI(Tl) and BaF_2, are shown in Fig. 3. In the calculation, the effect of the Doppler broadening mentioned earlier was taken into account and the experimentally measured cross sections and

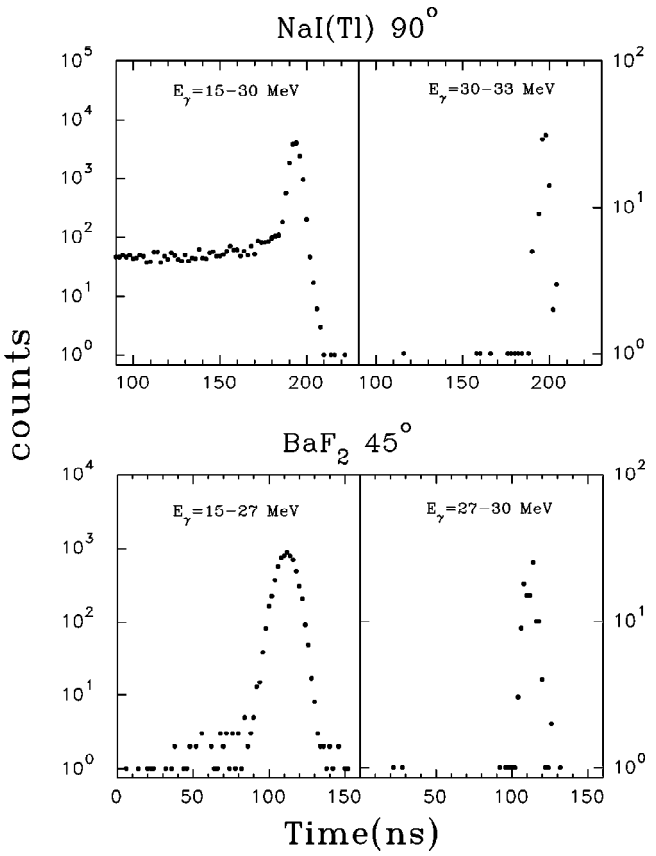

FIG. 2. Typical ZCOT spectra (used in the pileup rejection) for the NaI(Tl) detector at 90° and a BaF_2 detector at 45° for the energy gates shown in the figure.

angular distributions [16,17] for the $^{12}C(p,p'\gamma)$ reaction were utilized. The ratio of the experimental and calculated yields in the peak regions of the spectra (width ~ 1.8 MeV) is 0.84 ± 0.18 for both types of detectors. Thus the absolute efficiencies of the detectors as calculated by EGS4 are accurate within the experimental uncertainties which is mainly contributed by the error in the inelastic cross section ($\pm 20\%$) mentioned in Ref. [17]. Therefore, in folding the theoretical calculations and unfolding the experimental data over the entire gamma energy range, the response calculated from the EGS4 was utilized.

The gamma spectra obtained by projection from the list mode data after applying the necessary cuts on the TOF and ZCOT parameters and corrections for the random and residual pileup background are shown in Fig. 4(a) for the NaI(Tl) detector at 90° and in Fig. 4(b) for the BaF_2 detectors at three angles. The unfolded spectra for both NaI(Tl) and BaF_2 detectors at 90° agreed well in shape beyond ~ 12 MeV. There is a discrepancy of $\sim 20\%$ in absolute magnitude, part of which is due to the unfolding procedure. However, since the NaI(Tl) detector was having a better response for the highest energy gamma rays measured in this work, we have normalized the unfolded BaF_2 spectrum to the NaI(Tl) spectrum in the 12 MeV region. The unfolded spectrum shown in Fig. 5 is from the BaF_2 spectrum up to 12 MeV (after applying the normalization factor of 1.2) and from the NaI(Tl) spectrum for $E_\gamma > 12$ MeV. This spectrum

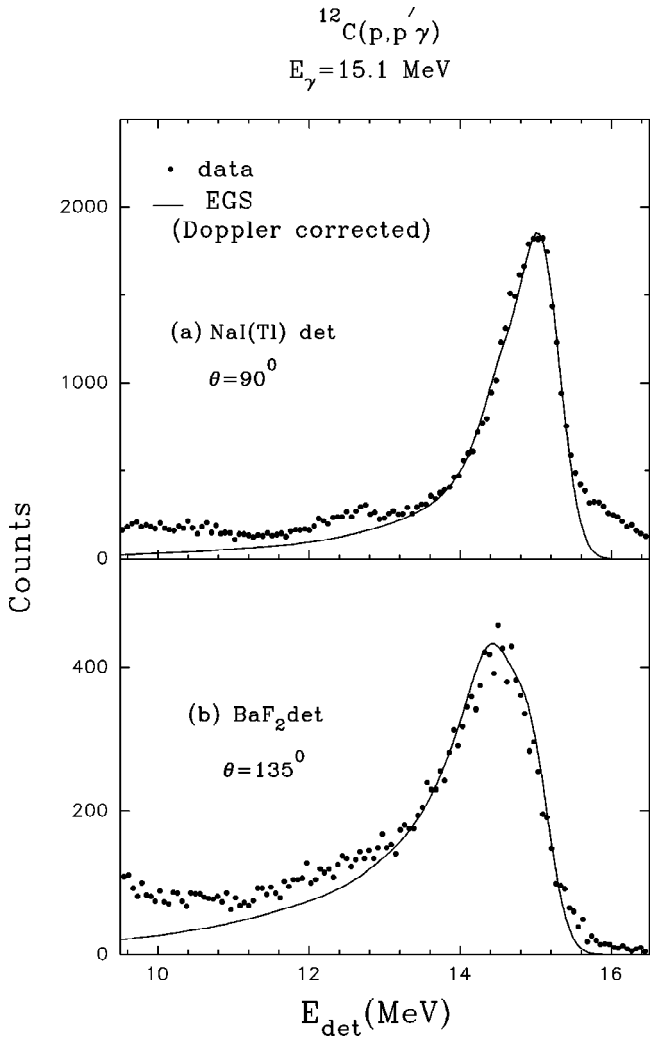

FIG. 3. Measured line shape for the 15.1 MeV line originating from $(p,p'\gamma)$ on ^{12}C at $E_p = 27$ MeV, in the NaI(Tl) detector at 90° and a BaF_2 detector at 135°. The solid lines show the prediction of EGS4 calculation after incorporating the Doppler correction (see text).

is used later only to compare with the prediction of the statistical and bremsstrahlung models. For the quantitative comparison of the energy spectrum at 90° with the DSD model, the calculation was folded with the NaI(Tl) response function. For the comparison of the angular distribution data, the calculations were folded with the BaF_2 response function.

III. STATISTICAL MODEL AND NUCLEON-NUCLEON BREMSSTRAHLUNG CALCULATIONS

The statistical model (SM) calculations were done with the modified version of the code CASCADE [18] incorporating the giant dipole resonance (GDR) built on excited states. The GDR energy and width were taken as 13.0 and 6.0 MeV, respectively, and the input fusion cross section was from the default choice in CASCADE, which gave 1925 mb. The level density prescription was that of Reisdorf, as elaborated on in Ref. [19], and the asymptotic liquid drop value of $\tilde{a}$ parameter was varied from $A/9$ to $A/15$ MeV^{-1}. Figure 5 shows the

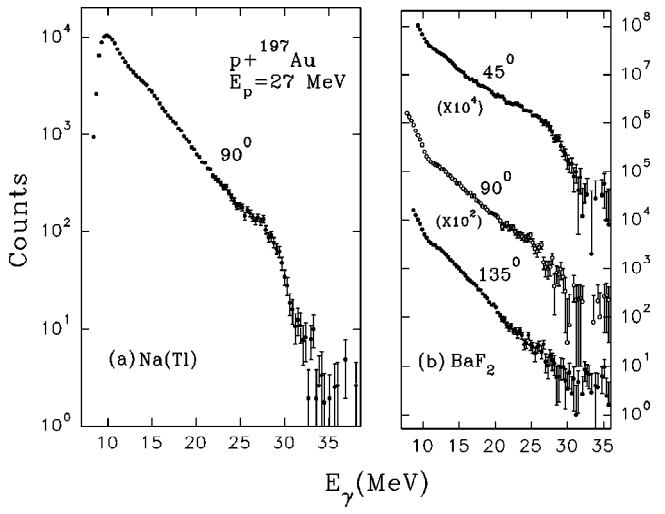

FIG. 4. Gamma spectra obtained after off-line analysis and correcting for neutron and pileup events (a) measured in the NaI(Tl) detector at 90° and (b) measured in the BaF_2 detectors at various angles.

predictions (SM1 and SM2) of the SM calculations for these two extreme choices of $\tilde{a}$. Clearly the SM model fails to explain the measured cross sections, particularly, for $E_\gamma > 12$ MeV.

The nucleon-nucleon bremsstrahlung (NNB) calculations were done following exactly the same procedures as in a previous work on alpha-induced gamma production on various targets [1]. The prescription of Nakayama and Bertsch [20] for the first chance collision was used. The high energy part of the spectrum arises in this model as a consequence of

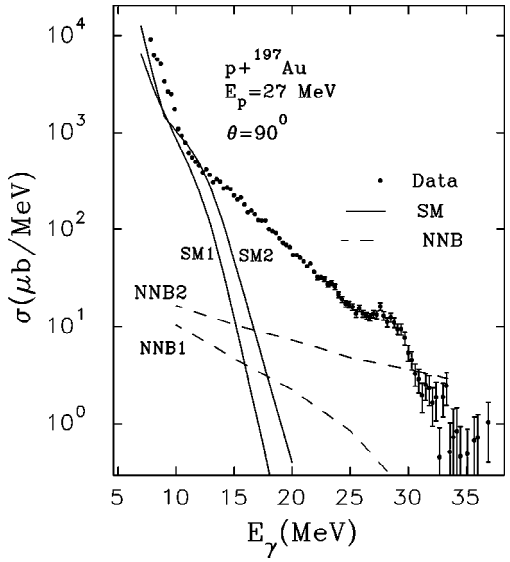

FIG. 5. Unfolded gamma spectra at 90°. The data beyond 12 MeV are derived from NaI(Tl) spectra and data up to 12 MeV are from the BaF_2 detector. The results of the SM calculation for two choices of the level density parameters $\tilde{a}=A/9$ (SM1) and $A/15$ (SM2) are shown by the solid lines. The dashed lines show the results of the NNB calculations for two different choices of momentum distribution in the target (see text).

the boost in the effective energy of collision (between the incoming proton and mainly the target neutrons), due to the Fermi motion of nucleons in the target. The Pauli blocking in the final scattering state produces a general decrease of cross section at higher E_γ. For the momentum distribution in the target we have used (1) a sharp-cutoff distribution with $k_F = 1.36\,\mathrm{fm}^{-1}$ and (2) a diffuse distribution with parameters suggested by Casas *et al.* [21]. The results of these calculations for $\theta_\gamma = 90°$ are shown in Fig. 5 (NNB1 and NNB2). Again it can be concluded that the NNB model fails to reproduce the measured cross sections (except, perhaps, at the highest energy region of the spectrum).

IV. DIRECT-SEMIDIRECT MODEL CALCULATIONS

The DSD model has so far been extensively applied for calculating the nucleon capture to discrete and bound final states. Recently it was extended to include capture to unbound states and used for calculating the gamma spectrum in proton capture on ^{89}Y at ~ 20 MeV [9]. In this section, we present the DSD model calculation of the gamma spectra for the present reaction $p + {}^{197}$Au at 27 MeV and compare with our measured data. The method of the calculation for capture to unbound states is similar to that described by Weller *et al.* [22]. However, our treatment of the unbound states in terms of quasibound states and resonances in the potential well of the target is different from that of Ref. [9].

In the DSD model, the incoming proton is captured either directly or via the intermediate excitation of a giant resonance into a final single particle configuration. The final configuration can be either a discrete bound state or an unbound state which can mix with the underlying continuum states. The differential cross section for the direct capture of a proton to a particular bound single particle state in the potential well of the target can be written as

$$\frac{d\sigma}{d\Omega} = \frac{Me^2 k_\gamma (2j+1)}{2\hbar^2 k'^3} \sum_\mu \left\{ \left| \sum_L A_{L\mu} D^L_{\mu 1}{}^* \right|^2 + \left| \sum_L A_{L\mu} D^L_{\mu -1} \right|^2 \right\}, \tag{1}$$

where

$$A_{L\mu} = i^{l'-L-l} B_L \sqrt{(2L+1)} \sum_{j'l'} C_0(jLj') C_\mu(jLj') I^{jl}_{j'l'}, \tag{2}$$

$$B_L = \sqrt{\frac{L+1}{L(2L+1)}} \; \frac{k_\gamma^L}{(2L-1)!!}, \tag{3}$$

$$C_\mu(jLj') = \langle j\,1/2 - \mu L\,\mu | j'\,1/2 \rangle, \tag{4}$$

$$I^{jl}_{j'l'} = \int u_{lj}(r) O_{EL}(r) \phi_{l'j'}(r) dr. \tag{5}$$

Here M is the proton reduced mass, $k_\gamma = E_\gamma/\hbar c$, k' is the wave vector of the incoming proton, L is the multipolarity of the electromagnetic transition (we consider only EL up to

$L=4$), C_μ in Eq. (4) represents the Clebsch-Gordan coefficient, and $D^L_{\mu\nu}$ are the D-matrix elements [23]. In the integral in Eq. (5), O_{EL} is the EL-transition operator, $u_{lj}(r)$ is the radial wave function of the final state with orbital and total angular momenta l and j, and $\phi_{l'j'}$ is the radial part of the incoming proton with angular momenta l' and j'. The summation over l' and j' in Eq. (2) is for all allowed values for a given L. The EL operator is given by [22]

$$O_{EL}(r)=\epsilon_L\frac{(2L+1)!!}{(L+1)k_\gamma^L}[(L+1)j_L(k_\gamma r)-k_\gamma r j_{L+1}(k_\gamma r)], \tag{6}$$

where j_L is the spherical Bessel function of order L and ϵ_L is the proton effective charge for electric multipole transition given by

$$\epsilon_L=\left(\frac{A_pA_T}{A_p+A_T}\right)^L\left[\frac{Z_p}{A_p^L}+(-1)^L\frac{Z_T}{A_T^L}\right], \tag{7}$$

Z_p and A_p being the charge and mass number of the projectile (here both are 1.0) and Z_T and A_T are those for the target. As can be seen we have used the ''density form'' of operators since the calculations are simpler. Moreover, the differences between this and the one using the ''current form'' are generally small [9]. The radial part u_{lj} is normalized as $\int|u_{lj}(r)|^2dr=1.0$ and calculated using a single particle potential with parameters discussed later. The wave function $\phi_{l'j'}$ is calculated using the optical model potential (OMP) which describes the proton elastic scattering cross sections on ^{197}Au. The choice of the OMP will also be discussed later. The normalization, in magnitude and phase, of this wave function is obtained by matching with the standard Coulomb wave functions G_l and F_l at large r. The former is obtained by integrating the radial Schrödinger equation outward from $r=0$.

When we consider the capture of the incoming proton to an unbound final state, the state can be a resonance or a nonresonant state. For a resonance state the total differential cross section can be obtained by integrating the double differential cross section $d^2\sigma/dE_\gamma d\Omega$ over the resonance. This double differential cross section for a direct capture to a final state can be written as

$$\frac{d^2\sigma}{d\Omega dE_\gamma}=\frac{M^2e^2k_\gamma(2j+1)}{\pi\hbar^4k'^3k}\sum_\mu\left\{\left|\sum_L A_{L\mu}D^L_{\mu1}{}^*\right|^2+\left|\sum_L A_{L\mu}D^L_{\mu-1}\right|^2\right\}, \tag{8}$$

where k is the wave number corresponding to the center of mass energy of the proton in the final state. All other quantities in Eq. (8) are similar to those in Eq. (1) except for the integral which is given by

$$I^{jl}_{j'l'}=\int\phi_{lj}(r)O_{EL}(r)\phi_{l'j'}(r)dr, \tag{9}$$

where ϕ_{lj} is the final unbound state wave function calculated by using a suitable potential. The normalization of ϕ_{lj} is same as that of $\phi_{l'j'}$ describing the initial state.

The modification of the above formulas when one considers also the semidirect capture process will be to replace the electromagnetic operator O_{EL} of Eq. (6) by $K_L(r)$ where

$$K_L(r)=O_{EL}(r)+\frac{F_L(r)}{E_\gamma-E_R+i\Gamma_R/2}, \tag{10}$$

E_R and Γ_R being the energy and width of the giant resonance of the corresponding multipolarity. In our calculation we have considered only the isovector GDR and the isoscalar and isovector giant quadrupole resonance (GQR). The function $F_L(r)$ for the semidirect isovector excitation can be written as [9]

$$F_L(r)=-\tau_3\frac{\hbar^2}{m}\frac{L(2L+1)}{E_R}\frac{NZ}{A^2}\frac{\langle r^{2L-2}\rangle}{\langle r^{2L}\rangle}f_{\rm sum}r^LV_1(r), \tag{11}$$

where N, Z, A refer to the target, $\tau_3=-1$ for proton, and $f_{\rm sum}$ is the fraction of sum rule strength of the corresponding multipole excitation. The radial average $\langle r^N\rangle$ was approximated as $3R^N/(N+3)$ where R is the uniform density radius. $V_1(r)$ is the isovector potential between the proton and the target which is responsible for the multipole excitation. As seen from Eq. (11), we have used a real isovector potential and the volume form for the particle-vibration coupling in the DSD model.

The function $F_L(r)$ for the semidirect isoscalar GQR excitation was taken as [9]

$$F_L(r)=-\frac{\hbar^2}{2m}\frac{L(2L+1)}{E_R}\frac{Z}{A}\frac{\langle r^{2L-2}\rangle}{\langle r^{k+L-2}\rangle}f_{\rm sum}\frac{r^{k-1}}{k+L+1}\frac{dU(r)}{dr}, \tag{12}$$

with the parameter $k=2$, consistent with the Tassie model [9]. The potential $U(r)$ is the total OMP discussed below.

The form of the OMP needed in calculating the incoming proton wave function and the isoscalar GQR coupling was taken as

$$U(r)=-U_R(r)-iU_W(r)+V_C(r), \tag{13}$$

where

$$U_R(r)=V_Rf(r,R_R,a_R)-4V_{\rm so}(\vec{l}\cdot\vec{s})\frac{1}{r}\frac{d}{dr}f(r,R_R,a_R), \tag{14}$$

$$U_W(r)=W_Vf(r,R_V,a_V)-4a_SW_S\frac{d}{dr}f(r,R_S,a_S), \tag{15}$$

with

$$f(r,R,a)=\frac{1}{1+\exp[(r-R)/a]}. \tag{16}$$

$V_C(r)$ is the Coulomb potential of a uniformly charged sphere of radius $R_C = 1.25A_T^{1/3}$. The potential parameters were taken from the compilation of Perey and Perey [24]. The sets chosen were those which describe the proton elastic scattering data on ^{197}Au at 28 MeV. Out of the four sets mentioned in the compilation, one particular set was seen to describe our data better than than the other three. The parameters were

$$V_R = 50.0\,\text{MeV}, \quad R_R = 1.24A_T^{1/3}\,\text{fm}, \quad a_R = 0.57\,\text{fm},$$

$$V_{so} = 8.6\,\text{MeV}, \quad W_V = 2.83\,\text{MeV}, \quad R_V = 1.22A_T^{1/3}\,\text{fm},$$

$$a_V = 1.60\,\text{fm}, \quad W_S = 4.78\,\text{MeV}, \quad R_S = 1.52A_T^{1/3}\,\text{fm},$$

$$a_S = 2.32\,\text{fm}.$$

The global Becchetti-Greenlees OMP (mentioned in the same compilation) was also not as successful. The choice of the isovector potential in Eq. (11) was consistent with the OMP systematics and its depth was taken as 24.0 MeV. The GDR energies and widths were taken from the ground state systematics [25] as $E_R = 13.7$ MeV and $\Gamma_R = 4.7$ MeV. The corresponding values for the isoscalar GQR were taken as 10.8 and 3.0 MeV and for the isovector GQR as 22.0 and 6.0 MeV. The sum rule strengths in Eqs. (11) and (12) were taken as 100% of the classical sum rule strength.

The choice of the potential for calculating the bound state wave functions was guided by the systematics [26]. This was taken as

$$V(r) = -V_0 f(r,R,a) + 4V_{so}(\vec{l}\cdot\vec{s})\frac{1}{r}\frac{d}{dr}f(r,R,a) + V_C(r), \tag{17}$$

with $V_0 = 57.5$ MeV, $R = 1.27A_T^{1/3}$ fm, $a = 0.67$ fm, and $V_{so} = 9.9$ MeV. $V_C(r)$ is the Coulomb potential as described above. In order to make a smooth transition from the bound states to unbound resonances with the increase in excitation energy, the same potential parameters were also used for the unbound resonances as well as for nonresonant continuum states. This potential gives 5 bound and 14 single particle resonances of different (l,j) values up to the resonance energy of $\sim$17 MeV (corresponding to gamma energy down to $\sim$10 MeV) as shown in Table I. The lowest 6 resonances have energies well below the combined Coulomb and the centrifugal barrier and qualify to be treated as ''quasibound'' states. Although the wave function of these states is of an undamped oscillatory nature for large r, its magnitude outside is very small compared to that inside the potential well. Thus for the purpose of calculating the radial integral the final state wave function can be treated as that of a bound state and normalized to unity by utilizing a cutoff distance outside the region of potential barrier. The check is that the results of calculation should be practically independent of the choice of the cutoff distance. This way of handling the final state makes the calculation simpler compared to that for an unbound resonance which we discuss below.

TABLE I. Bound and resonant single particle proton states. Negative $E_{\text{c.m.}}$ signifies a bound state. E_γ is the γ-transition energy. Γ_1 and Γ_2 are widths for two spreading options (see text) quoted for $E_\gamma > 20$ MeV.

State	$E_{\text{c.m.}}$ (MeV)	E_X (MeV)	E_γ (MeV)	$\Gamma 1$ (MeV)	$\Gamma 2$ (MeV)
$1d_{3/2}$	−6.31	0.79	33.13	0.16	0.16
$2s_{1/2}$	−5.86	1.24	32.68	0.37	0.37
$0h_{9/2}$	−2.11	4.99	28.92	2.98	2.40
$1f_{7/2}$	−1.42	5.68	28.24	3.48	2.74
$0i_{13/2}$	−0.86	6.24	27.68	4.98	3.86
$2p_{3/2}$	1.48	8.58	25.33	4.13	3.06
$1f_{5/2}$	1.56	8.66	25.26	4.40	3.25
$2p_{1/2}$	2.65	9.65	24.17	4.52	3.29
$1g_{9/2}$	5.45	12.55	21.36	5.92	4.16
$0j_{15/2}$	6.08	13.18	20.73	8.59	5.99
$0i_{11/2}$	6.30	13.40	20.52	6.42	4.47
$2d_{5/2}$	8.17	15.27	18.64	-	-
$3s_{1/2}$	9.17	16.27	17.64	-	-
$1g_{7/2}$	9.46	16.56	17.35	-	-
$2d_{3/2}$	9.88	16.98	16.94	-	-
$1h_{11/2}$	12.12	19.22	14.70	-	-
$0k_{17/2}$	13.36	20.46	13.46	-	-
$0j_{13/2}$	15.21	22.31	11.61	-	-
$1h_{9/2}$	16.91	24.01	9.91	-	-

The differential cross sections for transition to resonances were calculated by integrating the double differential cross section over the resonance as mentioned earlier. The integral in Eq. (9) for calculating this involves two unbound state wave functions which oscillate out to infinity. For the resonances which are not very much below the potential barrier as well as for the transition to the nonresonant continuum region, a direct numerical integration of this is impractical. We have followed the procedures of Ref. [22] and evaluated the integral by going over to the complex r domain. For the transition to the nonresonant continuum, the cross section is very small compared to those to the resonances (see later). It is clear that a calculation of the gamma spectrum corresponding to the transitions to the unbound states done in some finite energy steps may miss the resonances if these steps are much larger than the resonance widths. In our procedure, first we have calculated the resonance positions and then have calculated the $d\sigma/dE$ in narrow steps (typically 0.1 of the width) over the resonance. In the present case the single particle resonance widths were much smaller than 0.5 MeV except for the highest energy one in Table I which was about 1.5 MeV wide. For the energy regions between the resonances the calculations were done in steps of 0.5 MeV. To summarize, the calculations for the unbound region were done with three types of final states, viz., quasibound states, resonances, and nonresonant continuum.

The single particle (s.p.) states mentioned above are not the eigenstates of the full nuclear hamiltonian. The s.p. strengths are fragmented or continuously spread over the underlying complex continuum states. An understanding of this

damping of the s.p. strength is important. In principle, if the DSD model is the correct description of gamma production in proton capture, one should be able to extract information about the s.p. states from the measured gamma spectrum. In our work before comparing with the experimental spectrum, the calculated cross sections for transitions to the single particle states were spread out. The spreading was done by assigning a width to each state. The width was calculated, to first order in perturbation, as $\Gamma = 2\langle W \rangle$ where W is the imaginary potential for the final states and the expectation value was taken using the corresponding single particle wave functions. It should be noted that we have ignored the imaginary potential while calculating the wave functions. In this picture the role of W is only to spread the s.p. strength. For the exclusive experimental cross sections in coincidence with the decay products of the final states, this may not be justified. The form factor of W was taken as a derivative Woods-Saxon with the radius and diffuseness parameters the same as those of the single particle potential. The strength W_0 was taken as

$$W_0 = A + BE, \tag{18}$$

where A and B are parameters and E is the resonance energy (in MeV). For the calculation of the widths of the bound states, the continuation of the effective imaginary potential for the negative energy states was done following the same procedure as in Ref. [9] as

$$W_0 = \frac{a(E-E_0)^2}{b+(E-E_0)^2}, \tag{19}$$

with $E = -E_b$, E_b being the binding energy and $E_0 = -S_p$ the proton separation energy of ^{198}Hg. The constants a and b are related to A and B in Eq. (18) so as to make the value and slope of W_0 continuous at $E = 0$.

The spreading of the strength was done in two extreme ways. In one the calculated cross section for each state was spread with a Gaussian form factor characterized by the corresponding calculated width. In the other procedure, the single particle strength was distributed as Gaussian with the same width and the cross section was calculated for each final energy around the mean energy. However, the final state wave function was calculated by demanding a resonance or a bound state to occur at the shifted energy around the original state. This was done by slightly adjusting the potential depth. The calculated cross sections were then folded with the single particle strengths. For the same set of A and B parameters in Eq. (18) the second procedure gives a somewhat higher (by about a factor of 1.2–1.5) cross section.

In the actual procedure, first the cross sections for the bound, quasibound, resonant, and nonresonant continuum states are calculated. Figure 6 shows the contribution from the different bound and resonant states listed in Table I, with and without GQR excitation in the semidirect process. It is seen that the effect of including the GQR is small. In subsequent calculations, therefore, we have considered only the GDR in semidirect capture. The spreading width for each

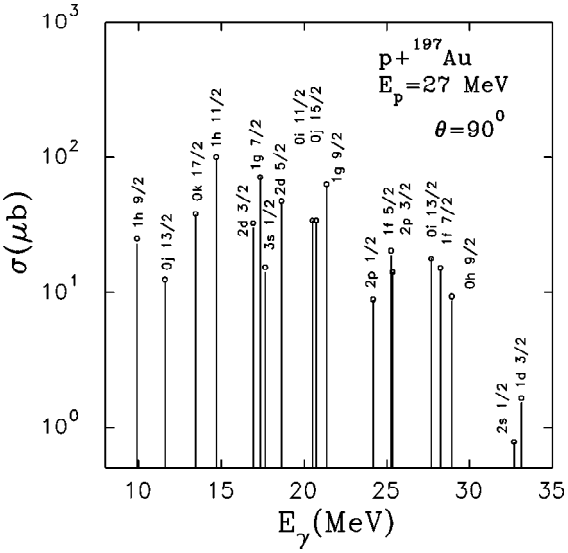

FIG. 6. Results of the DSD model calculation at 90°, incorporating only the GDR, for transitions to different bound and resonance states mentioned in Table I. The open circles show the results after including the isoscalar and isovector GQR.

state was then calculated as described above and the calculated cross sections after spreading were folded with detector response before comparing with the data. The parameters A and B in Eq. (18) were varied until a reasonably good description of the data is obtained. The calculated spectra are shown in Fig. 7 for both procedures of spreading mentioned above. It may be noted that there is no arbitrary normalization factor used before comparing with the data. The dotted curve in the figure shows the contribution coming from the nonresonant continuum states and is obviously negligible as mentioned earlier.

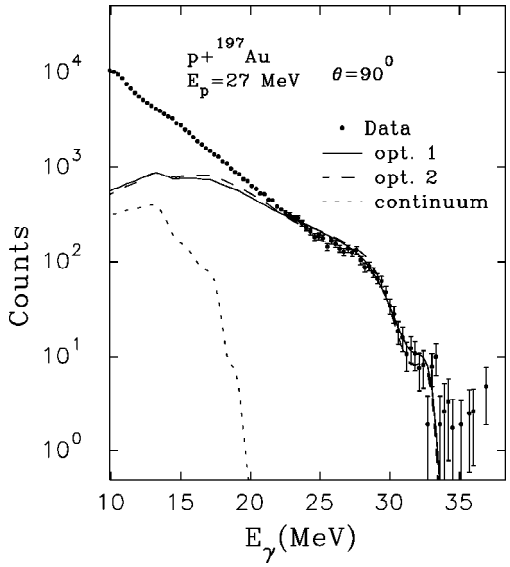

FIG. 7. Results of the DSD model calculation of the gamma spectrum, after spreading and folding with the NaI(Tl) detector response and comparison with data at 90°. The results of two spreading options (mentioned in the text) are shown. The dotted line shows the contribution from the continuum only.

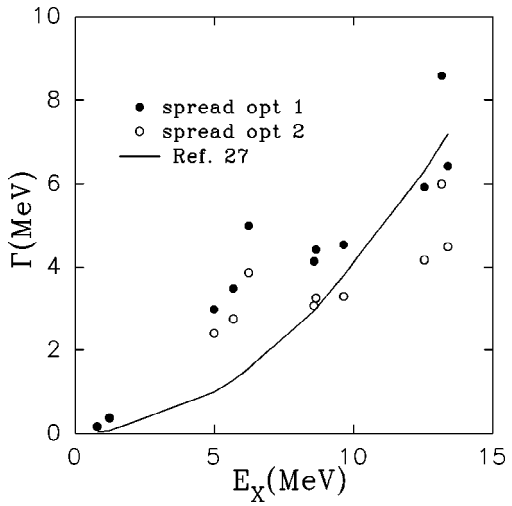

FIG. 8. Spreading widths of the single particle states in the two prescriptions 1 and 2 plotted against the excitation energy. Also shown is the prescription of Ref. [27].

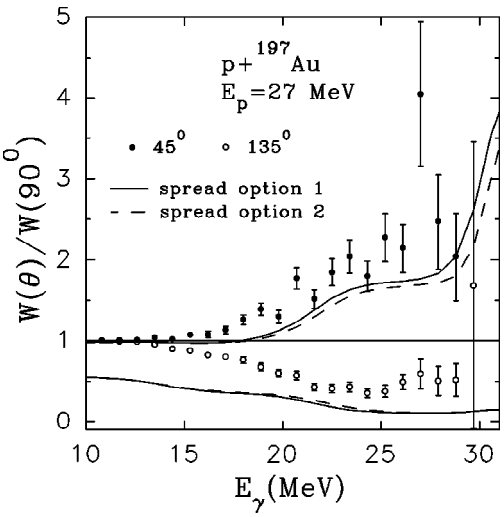

FIG. 9. Results of the DSD model calculations for the angular distribution after spreading and folding with BaF_2 detector response, and comparison with data.

From these figures, it appears that the DSD model is successful in describing the measured spectrum at 90° in the range $E_\gamma > 20$ MeV. There is not much difference in the predicted shape of the spectra for the two extreme choices of spreading procedure. However, the A and B parameters for the best fits are different, viz., 5.0 MeV and 0.38, and 3.8 MeV and 0.2, respectively, for the two choices. This means that the calculated widths of the single particle states are different as shown in Table I and Fig. 8. The actual description of spreading should probably be intermediate between these two extreme prescriptions. Also shown in Fig. 8 are the spreading widths calculated using the parametrization of empirical values derived from the existing data [27], which, however, fail to reproduce our measurements.

The main uncertainties in the DSD calculation are (a) the uncertainty in the initial and final state OMP parameters and (b) the model dependent width of the final s.p. configuration. Therefore in the present work we cannot claim to have extracted the single particle strength distribution from the data uniquely. The uncertainties in the extracted widths in our procedure is at least as much as the difference shown in Fig. 8 for the two options. Further systematic experiments at various beam energies and with better energy resolution (for example with large volume germanium detectors) to resolve the different particle bound states should shed more light on this aspect. In particular, measurements with closed shell target nuclei such as ^{208}Pb should be performed to establish the method, since the s.p. properties have been studied with various probes in such systems.

It is evident from Fig. 7 that the DSD model fails to describe data below 20 MeV. In fact the part of the spectrum from 12 to 20 MeV remains unexplained by any model mentioned earlier. As mentioned in Ref. [9] the role of multistep processes on a time scale faster than that of the compound nuclear processes should be important in this regime.

The calculated angular distributions are compared with the data in Fig. 9 for both methods of spreading. Here the angular distribution data are presented as $W(\theta)/W(90°)$ as a function of E_γ, where $W(\theta)$ is the spectra measured with the BaF_2 detector at the angle θ. Although the shape of the calculated energy variation of $W(45°)/W(90°)$ and $W(135°)/W(90°)$ agrees reasonably with the data for $E_\gamma > 20$ MeV, there is disagreement in magnitude. It might be pointed out that a similar discrepancy is present in the data of Parker *et al.* [9] and needs to be understood.

V. SUMMARY

We have measured the gamma production cross sections as a function of gamma energy at various angles in the reaction $p + {}^{197}$Au at $E_p = 27$ MeV. The statistical model fails above 12 MeV and the contribution from the nucleon-nucleon bremsstrahlung process is insignificant almost throughout the spectrum. The direct-semidirect model is reasonably successful in describing the data for the high energy part of the spectrum between ~20 and 33 MeV. The prediction of the angular dependence of cross sections is not as good as that for the spectrum at 90° but reproduces the trend. The multistep reactions should be important for the 12–20 MeV range. The present work has also illustrated the possibility of extracting information on the single particle strengths in heavy nuclei from such particle capture reactions. A systematic study for different beam energies will be necessary to extract more accurate results on this aspect.

We would like to thank the crew at the Nuclear Science Centre for the excellent operation of the Pelletron accelerator.

[1] M. K. Sharan, Y. K. Agarwal, C. V. K. Baba, D. R. Chakrabarty, and V. M. Datar, Phys. Rev. C **48**, 2845 (1993).
[2] J. A. Behr, K. A. Snover, C. A. Gossett, G. Feldman, J. H. Gundlach, and M. Kicinska-Habior, Phys. Rev. C **53**, 1759 (1996).
[3] M. Kwato Njock, M. Maruel, H. Nifenecker, J. Pinston, F. Schussler, D. Barneoud, S. Drissi, J. Kern, and J. P. Vorlet, Phys. Lett. B **207**, 269 (1988).
[4] J. A. Pinston, D. Barneoud, V. Bellini, S. Drissi, J. Guillot, J. Julien, M. Kwato Njock, H. Nifenecker, M. Maruel, F. Schussler, and J. P. Vorlet, Phys. Lett. B **218**, 128 (1989).
[5] J. Clayton, W. Benenson, M. Cronqvist, R. Fox, D. Krofcheck, R. Pfaff, T. Reposeur, J. D. Stevenson, J. S. Winsfield, B. Young, M. F. Mohar, C. Bloch, and D. E. Fields, Phys. Rev. C **45**, 1815 (1992).
[6] C. A. Gossett, M. S. Kaplan, S. J. Luke, B. T. McLain, R. Vandenbosch, and D. P. Wells, Nuclear Physics Laboratory Annual Report, University of Washington, 1992, p. 17.
[7] G. E. Brown, Nucl. Phys. **57**, 339 (1964).
[8] C. F. Clement, A. M. Lane, and J. R. Rook, Nucl. Phys. **66**, 273 (1965); **66**, 293 (1965).
[9] W. E. Parker, M. B. Chadwick, F. S. Dietrich, J. E. Kammeraad, S. J. Luke, K. E. Sale, R. M. Chasteler, M. A. Godwin, L. H. Kramer, G. J. Schmid, H. R. Weller, and A. K. Kerman, Phys. Rev. C **52**, 252 (1995).
[10] Obtained from Bicron Corporation, 12345 Kinsman Road, Newbury, Ohio 44065.
[11] I. Mazumdar, P. Sugathan, J. J. Das, D. O. Kataria, N. Madhavan, and A. K. Sinha, Nucl. Instrum. Methods Phys. Res. A **417**, 297 (1998).
[12] Obtained from Quartz & Silice Holland B. V., Rijnzathe 4, 3454 ZK De Meern, The Netherlands.
[13] W. R. Nelson, H. Hirayama, and D. W. O. Roger, Stanford University Report No. SLAC-265, 1985.
[14] H. V. Geramb, K. Amos, R. Sprickmann, K. T. Knopfle, M. Rogge, D. Ingham, and C. Mayer-Boricke, Phys. Rev. C **12**, 1697 (1975).
[15] S. M. Austin, P. J. Locard, S. N. Bunker, J. M. Cameron, J. Reginald Richardson, J. W. Verba, and W. T. H. van Oers, Phys. Rev. C **3**, 1514 (1971).
[16] R. H. Howell, F. S. Dietrich, and F. Petrovich, Phys. Rev. C **21**, 1158 (1980).
[17] D. Berghofer, M. D. Hasinoff, R. Helmer, S. T. Lin, and D. F. Measday, Nucl. Phys. **A263**, 109 (1976).
[18] F. Puhlhofer, Nucl. Phys. **A280**, 267 (1977).
[19] M. Kicinska-Habior, K. A. Snover, C. A. Gossett, J. A. Behr, G. Feldman, H. K. Glatzel, J. H. Gundlach, and E. F. Garman, Phys. Rev. C **36**, 612 (1987).
[20] K. Nakayama and G. F. Bertsch, Phys. Rev. C **34**, 2190 (1986).
[21] M. Casas, J. Martorell, E. Moya de Guerra, and J. Treiner, Nucl. Phys. **A473**, 429 (1987).
[22] H. R. Weller *et al.*, Phys. Rev. C **25**, 2921 (1982).
[23] M. E. Rose, *Elementary Theory of Angular Momentum* (Wiley, New York, 1957).
[24] C. M. Perey and F. G. Perey, At. Data. Nucl. Data Tables **17**, 1 (1976).
[25] S. S. Dietrich and B. L. Berman, At. Data Nucl. Data Tables **38**, 199 (1988).
[26] A. Bohr and B. R. Mottelson, *Nuclear Structure* (Benjamin, New York, 1975), Vol. 1.
[27] C. Mahaux and R. Sartor, *Advances in Nuclear Physics* (Plenum, New York, 1991), Vol. 20.